

Vibrational Spectroscopy Techniques Used in the Analysis of Glycation Products, Water Content in the Dermis of Diabetic Elderly, Healthy Young, Healthy Elderly Women, and in the Interpretation of Goiter, Follicular and Papillary Thyroid Cancer

Claudio Téllez Soto, A.^{1*}, Liliane Pereira Pinto², Lázaro Medeiros Neto, P.¹, Claudio Téllez Zepeda, A.¹, Michely Silva, G. P.¹, Isamara Tanaka³ & Airton Martin, A.¹

¹*Biomedical Engineering Innovation Center – Biomedical Vibrational Spectroscopy Group. Universidade Brasil – UBr – Rua Carolina Fonseca, 235 – 08230-030 – Itaquera • São Paulo/SP, Brasil*

²*FEPI-Fundação de Ensino e Pesquisa de Itajubá, Centro Universitário de Itajubá. Av. Dr. Antônio Graga Filho, 687-Porto Velho, Itajubá-MG, 35501-002. Brasil*

³*Hospital São Francisco de Assis–Coordenadora da UTI pediátrica.– Rua Ernesto Duarte, 70 CEP 12311-200. Parque Califórnia–Jacareí-SP. Brasil*

***Correspondence to:** Dr. Claudio Téllez Soto, A., Biomedical Engineering Innovation Center - Biomedical Vibrational Spectroscopy Group, Universidade Brasil - UBr. São Paulo, Brazil. Email: cayotellez@gmail.com

Copyright

© 2022 Dr. Claudio Téllez Soto, A., *et al.* This is an open access article distributed under the Creative Commons Attribution License, which permits unrestricted use, distribution, and reproduction in any medium, provided the original work is properly cited.

Received: 15 April 2022

Published: 29 April 2022

Keywords: *Vibrational Spectroscopic Techniques; Dermal Glycation Products; Dermal Water Content; Diabetic Elderly; Healthy Young; Healthy Elderly Women; Thyroid Cancer; Goiter*

Abstract

In this article we present several vibrational spectroscopic techniques used in the analysis of glycation products and water content in the dermis of diabetic elderly, healthy young, and healthy elderly women, as well as in different types of thyroid cancer, goiter and abnormal lymph nodes. The measurements of the different samples were made using confocal Raman spectroscopy and Fourier transform infrared spectroscopy. When necessary, vibrational assignments were performed

by theoretical calculation of the spectra based on the Density Functional Theory (DFT). The spectroscopic techniques were: correction of the spectra baseline, vector normalization, smoothing, second spectral derivative, band deconvolution analysis, spectral subtraction, spectral inversion, analysis of the intensity of the fundamental bands, enhanced infrared absorbance's and SERS effect.

Introduction

Over the past ten years, the research group of vibrational spectroscopy applied to biomedical engineering at Universidade Brasil (São Paulo) published a series of scientific articles related to cancerous tissues [1-5]. We also published studies concerning glycation products present in the dermis of young, healthy elderly and elderly women with diabetes [6-9], as well as the extension of these researches to the dermal water content using the comparative analysis of proline bands and hydroxyproline in the spectral region between 1000 - 800 cm^{-1} , and in the spectral region between 300-3600 cm^{-1} [10]. In the case of the confocal Raman spectroscopic study of papillary and follicular thyroid cancer, as well as goiter, the vibrational assignment of the Amide I bands was based on previous studies of the infrared spectra in relation to the protein composition of the cancerous tissue. In a previous study on the analysis of bacteria by infrared spectroscopy [11], we presented a spectra measurement technique that increases the absorbance by approximately 400%.

In the article [8], we employed RM1 semi-empirical and DFT: B3LYP/3-21G methods to achieve theoretical insights regarding the confocal Raman experimental observations in qualitative water content of the skin dermis of healthy young, healthy elderly and diabetic elderly women. It is well known that the water quantity in healthy human dermis increases with age. However, in the elderly diabetic group, the increased sugar content directly affects the proline and hydroxyproline bands as well as the dermal water content. In the present work, our first approach was to perform a theoretical model of these systems using the RM1 semi empirical method and, after the subsequent model was built using DFT/B3LYP:3-21G procedures considering the amino acids chain formed by hydroxyproline and proline alone, which interact with one and four water molecules, we analyzed the dipole moment and the polarizability variation in order to determine the hydrogen bonds in these systems.

In our paper “*In vivo* determination of dermal water content in chronological skin aging by confocal Raman spectroscopy” [10], the difference in the total water content between elderly diabetic women vs healthy young women, and for healthy elderly women vs healthy young women were of 2.7 and 1.6%, respectively. In order to analyze only bounded water (independent of the use of skin - tools) in the amino acids chain of collagen, we subtracted the Raman water spectrum from the mean Raman spectra for the three groups of participants.

In the publication “Combined *in vivo* confocal Raman spectroscopy and density functional theory to detect carboxymethyl(lysine) in the human stratum corneum” [6], the identification of CML in the set of experimental confocal Raman spectra of the skin of young, healthy elderly and diabetic elderly women was done by comparison with the confocal Raman spectrum of CML, with the calculated B3LYP/6-311G spectrum of CML, with the second derivative spectrum of the mean value of the confocal Raman spectra of the skin of the three groups of participants, and by comparing between the second derivative spectrum of the three groups of participants with the confocal Raman spectrum of CML. The differences between

the three groups of spectra were analyzed through band deconvolution analysis (BDA) and through the corresponding Gaussian fitting according to the relative concentrations of the CML spectral coincidental bands for each group.

In the paper “Infrared and confocal Raman spectroscopy to differentiate changes in the protein secondary structure in normal and abnormal thyroid tissues” [1] the histological analysis of normal thyroid tissue, goiter, papillary carcinoma, and follicular carcinoma samples, conducted in a mean time of 3 to 5 days, showed an intrinsic variance among them. By confocal Raman spectroscopy, a set of 100 spectra for each tissue sample was acquired in a few minutes. It is evident that diagnosis of goiter and thyroid cancer by means of confocal Raman spectroscopy is significantly faster in comparison to conventional approaches.

We used the Gaussian fitting of the Amide I band in the four types of samples. The band positions inside the profile of the Amide I band was determined using the second derivative and the FSD spectra. In both the IR and confocal Raman spectra, percentages of the different components of the secondary proteins' structure were found after three consecutive Gaussian fittings for each different group of samples. We showed the mean values obtained using this procedure, with the wavenumbers and area values given within the confidence interval.

In the article “Enhanced Infrared Absorption in a Comparative Study between Multi-Sensitive and Multiresistant Bacteria of the Genus *Klebsiella sp*” [11], we studied the infrared spectral profile of *Klebsiella sp* bacteria with respect to sensitivity and resistance. The differentiation between these organisms can properly guide the therapeutic conduct. We processed the samples obtained from the laboratory of Hospital Santos Dumont in a Mac Conckey culture medium. After that, we processed a micromass in order to provide a thin film for evaluation by means of FTIR spectroscopy. The pilot study was performed using both glass slides and glass slides coated with a copper sheet of 45 μm thickness as support for the samples. After the bibliographical review, we highlighted the relationship between the amino acid serine and bacterial resistance in this type of bacteria, which occurs through plasmids. We collected the spectra from 50 bacterial strains divided in two groups: 25 sensitive and 25 resistant strains on glass, and 21 sensitive and 21 resistant strains on the copper sheet. We obtained the composition of the samples by evaluating the spectra with multivariate analysis using the second derivative. We concluded that infrared spectroscopy could also be used to identify multiresistant *Klebsiella sp* by means of the amino acid serine, which can be considered as a marker found only in multiresistant forms.

Handling with lymph nodes, we wrote the article “Estudo de linfonodos por espectroscopia Raman confocal” [2], in which we aimed to identify the main biochemical characteristics in normal and compromised lymph nodes, and in cervix lesions, using confocal Raman spectroscopy. We used spectroscopic methods to analyze 12 normal and altered lymph node samples from patients with medical indication for lymphadenectomy. We performed the statistical analysis of the main components (PCA) and linear discriminant analysis (LDA) [12]. In a subsequent work on lymph nodes, we studied these kinds of tissues by means of the SERS effect [3], using the following technique: we prepared a support matrix for the samples on a glass slide that was covered with a thin layer of chitosan, on which we deposited silver nanoparticles.

Materials and Methods

1. Spectrophotometers: in most of the articles presented here, the instrumentation and measurement conditions were as follows: 1) Infrared spectra: we captured the spectra using a Spectrum 400 FT-IR (Perkin-Elmer) spectrometer equipped with a MCT (mercury cadmium telluride) detector in the region of 4000 to 400cm^{-1} , with gain of 1 and resolution of 4cm^{-1} . We recorded between 50 and 120 spectra. We took a background spectrum in order to subtract any possible interferences from the external environment, in some cases including the slide glass itself. 2) We used a confocal Raman system from River Diagnostics (River Diagnostics® model 3510 -Netherlands), with 785nm laser diode as the excitation source. The power on the sample was set to 20mW, and the exposure time was of 22 s (with accumulation of 1s). The laser spot was of approximately $2\mu\text{m}$, and the Raman signal was collected with a CCD detector.

Besides, in some cases we recorded the Raman spectra of the solid samples at room temperature with a Bruker Spectrometer (model RFS 100/S) equipped with a 1064 nm Nd:YAG laser as the excitation source. Acquisition parameters were: 500mW for laser power, spectral resolution of 4cm^{-1} , signal gain of 1, 200 scans and 7.0mm for aperture setting.

2. Computational devices: we used the following software: HYPERCHEM [13], GAUSSIAN 03 [14], and CHEMCRAFT 1.8 [15]. Theoretical structural calculations provided the structural parameters which we used to obtain the calculated vibrational spectra. The computations were carried out in a computer with the following configuration: Intel® Core™ i5 (1.80GHz) with 4GB of RAM.

Results and Discussion

i. Spectral Second Derivative and Fourier Self-Deconvolution (FSD) Analysis

The second spectral derivative is a spectroscopic technique used in order to obtain information about the hidden bands under broad and intense band profiles. The positions of the most intense peaks with negative values in the second derivative spectra also indicate how to proceed with the band deconvolution analysis. In the article on thyroid cancer, we used this technique applied to the Amide I bands. Thus, we analyzed the protein composition and inferred about its variations in different tissues. Figure 1 illustrates this procedure for normal thyroid tissue showing the second spectral derivative in blue, the Amide I band profile in black and the FSD in red.

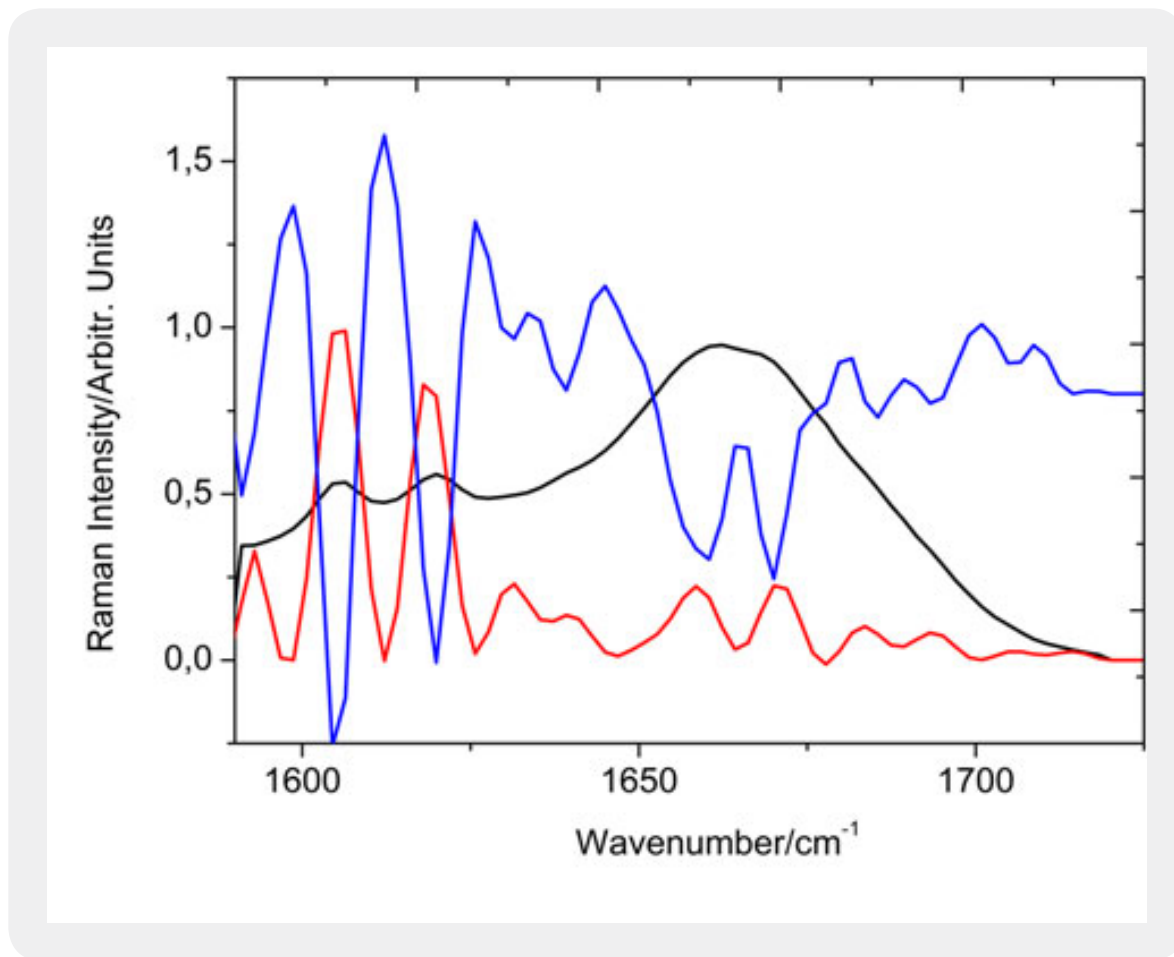


Figure 1: Amide I band profile in the normal thyroid tissue. Confocal Raman spectrum (black), second derivative spectrum (blue), and FSD spectrum (red) [1].

From Figure 1, we can conclude that the hidden bands between the second derivative and the FSD are coincident. On this graph, we warn some authors about the theoretical inconsistency of measuring the areas of the second derivative to infer concentration results for the different structural compositions of the Amide I band. For example, the bands designated as side chains, which appear at 1605 and at 1619 cm^{-1} , have nearly equal intensities in the Raman spectrum. Both in the second derivative and in the Fourier proper deconvolution, these bands show higher intensities. The second derivative bands are dimensionless and do not include concentration, which is an intensive variable. The mathematical expression of Raman intensities contemplates concentration.

ii) Inversion of the Second Derivative Spectra

The protein structure does not have a high point group, with several symmetry elements. On the contrary, due to its helical structure, composed of different types of amino acids, the only symmetry element of this structure is the identity, E. Hence, the symmetry selection rules in vibrational spectroscopy indicate the same

activity in both the Raman and the infrared spectra, which therefore coincide with respect to the number and position of the bands. The only difference that these spectra show is their intensity: symmetrical vibrations are most intense in the Raman spectrum and asymmetrical vibrations are most intense in the infrared spectrum. Since we had already recorded the infrared spectra of these tissues, we obtained their second derivatives and performed the inversion of the second derivatives of the Raman spectra in the spectral region between 1800 and 1550 cm^{-1} . Figure 2 illustrates the coincidence between the positioning of the bands in both spectra.

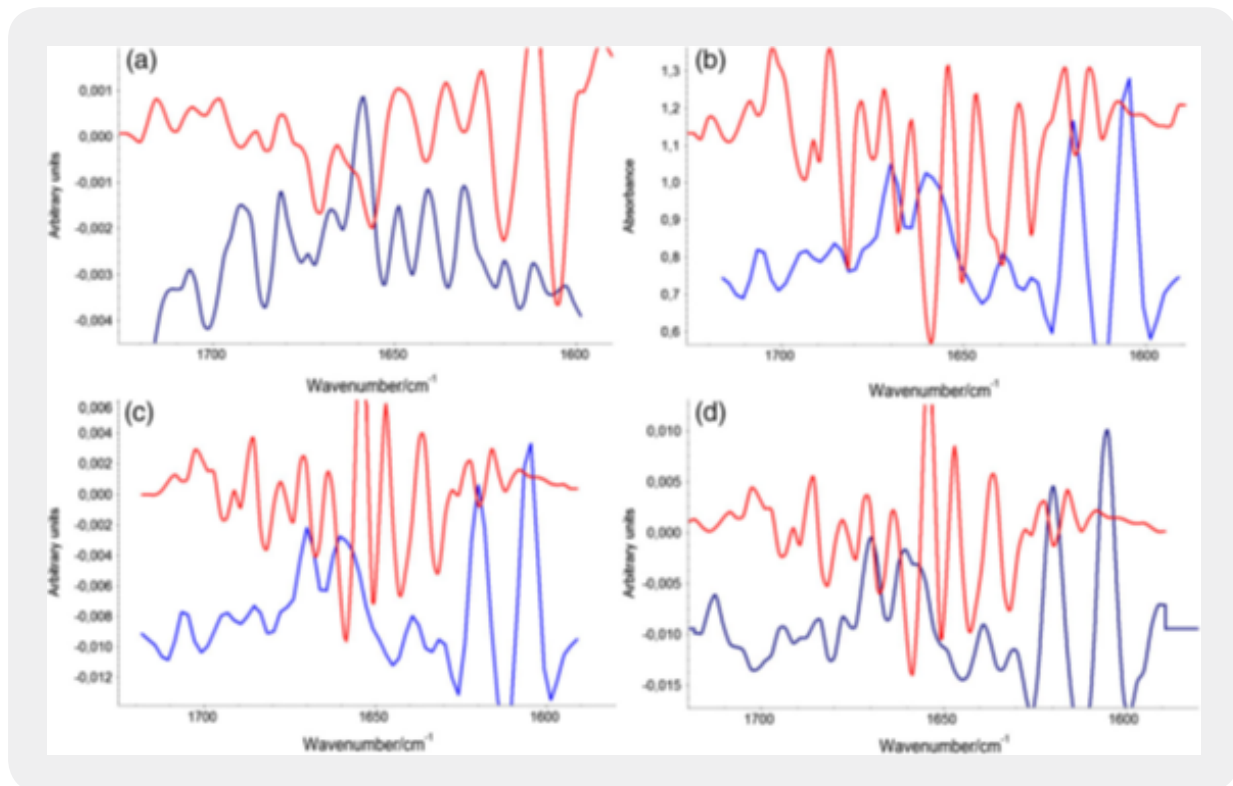


Figure 2: Comparative IR and confocal Raman second derivative spectra of the Amide I band of normal tissue, goiter, and carcinomas, in which the inverse of the second derivative of the confocal Raman spectra (in blue) is shown in order to facilitate visual comparison [1].

Conclusions

Table 1: Band assignments for the infrared spectra of normal tissue, goiter, follicular (FTC), and papillary thyroid carcinomas (PTC) in the Amide I region (1580 – 1725 cm⁻¹):

Normal wavenumber/cm ⁻¹		Goiter wavenumber/cm ⁻¹		FTC wavenumber/cm ⁻¹		PTC wavenumber/cm ⁻¹	
1623	β-sheet	1614	side chain	1621	β-sheet	1625	β-sheet
1623	β-sheet	1626	β-sheet	1621	β-sheet	1630	β-sheet
1634	β-sheet	1632	β-sheet	1633	β-sheet	1632	β-sheet
1641	β-sheet	1644	β-sheet	1642	β-sheet	1645	β-sheet
1649	random	1651	random	1651	random	1651	random
1658	α helix	1659	α-helix	1659	α-helix	1659	α-helix
1666	β-turn	1667	β-turn	1667	β-turn	1668	β-turn
1679	β-turn	1674	β-turn	1676	β-turn	1675	β-turn
1691	β-sheet	1682	β-turn	1681	β-turn	1681	β-turn
1707	Glu.v(C¼O)	1682	β-turn	1686	β-turn	1684	β-turn

From the deconvolution results, we achieved a clear differentiation between the confocal Raman spectra of the four sample groups. We can consider side chain bands as constant in normal thyroid tissue, papillary, follicular, and goiter, with percentage values of 16%, 15%, 14%, and 13%, respectively. The β-sheet bands predominate in normal thyroid tissue, with 20%, followed by the goiter samples, with 17%. For the papillary and follicular carcinomas, the percentages were of 15% and 14%, respectively. The α-Helix secondary protein structure was higher in the papillary carcinoma, with a percentage of 45% compared with the normal tissue (22%) and CFT samples (22%). The α-Helix structure was absent in the goiter samples. Goiter was the only sample which presented the 310-Helix structure with the highest percentage (56%) with a band located at 1661 cm⁻¹ [16,17]. The 310-Helix structure is also found in the normal tissue with 12% and in the follicular carcinoma with 16%. The β-turn secondary structure presents 28% in the normal tissue, 25% in the follicular carcinoma, and 24% in the papillary carcinoma. In goiter samples, the β-turn structure indicates 13%. Table S2 and Table 3 depict the Gaussian fitting and band areas in the Amide I spectral region between 1580 and 1720 cm⁻¹, as obtained from the confocal Raman spectra for the four groups of samples. As happens with the vibrational spectra of proteins, where there is no symmetry center or a specific point group (only the C1 group), the positions of the bands must coincide in the IR and Raman spectra, but with different intensities. Therefore, the corresponding assignments of the deconvolution bands was done mainly based on literature data for the IR spectra [16, 18–20].

III) Spectral Second Derivative and Gaussian Band Deconvolution

In the paper *RM1 semi-empirical and DFT: B3LYP/3-21G theoretical insights on the confocal Raman experimental observations in qualitative water content of the skin dermis of healthy young, healthy elderly and diabetic elderly women's* [8] that we took as a base for deconvolution band analysis, the second derivative spectra are indications for the Gaussian fitting, Lorentzian fitting, or for other deconvolution functions. The number of fitting bands must not exceed the number of indicative peaks found by the second derivative spectra, and the fitting procedure has to be repeated at least three times in order to obtain sound statistical parameters for the band deconvolution procedure. Figure 3 shows the band deconvolution analysis for the mean confocal Raman spectra of the diabetic elderly women (DEW), healthy elderly women (HEW), and

healthy young women (HYW) volunteers in the proline and hydroxyproline spectral region, and we present the second derivative spectra of the proline and hydroxyproline bands for these groups of participants.

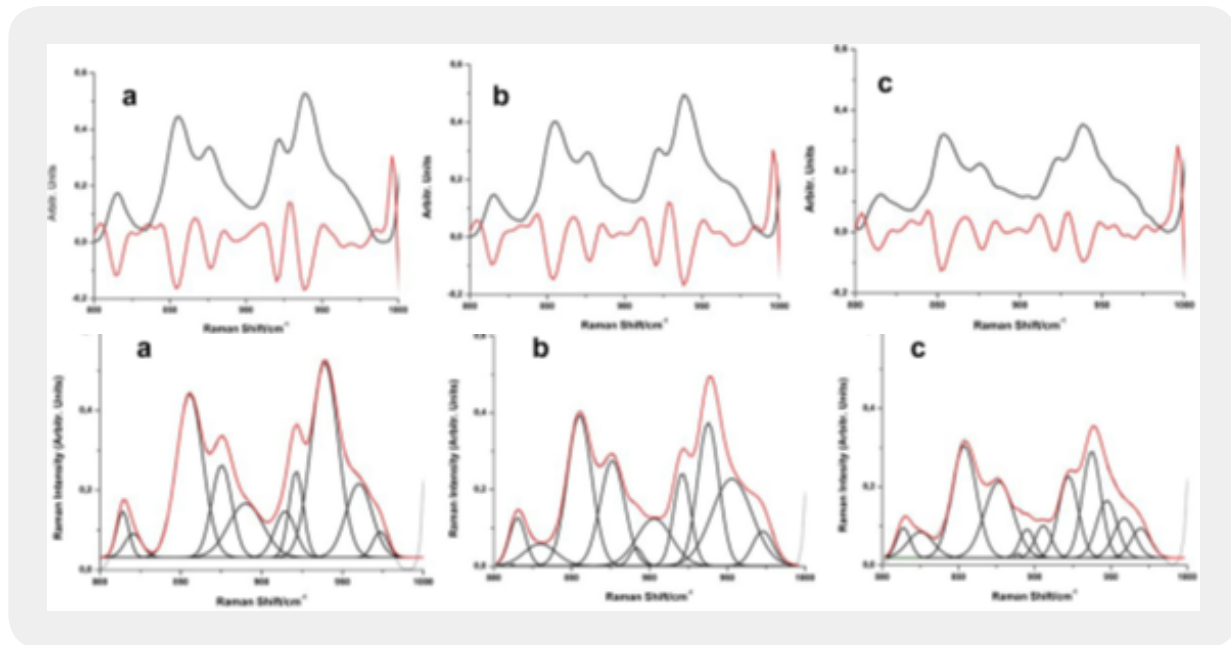


Figure 3: In red, the second derivative spectra of HYW (a), HEW (b), and DEW (c), in the spectral region of proline and hydroxyproline ($1000 - 800 \text{ cm}^{-1}$). In black, the band shape in the $1000 - 800 \text{ cm}^{-1}$ spectral region. At the bottom: band deconvolution analysis (Gaussian fitting) for the confocal Raman spectra of HYW (a), HEW (b), and DEW (c), in the spectral region of proline and hydroxyproline ($1000 - 800 \text{ cm}^{-1}$). Amide I normalization [8].

Conclusions

Nguyen *et al.*, 2013 [21] indicates the ratios of the integrate intensities for the vibrational modes in the Amide I region. In our case, the following integrate intensities were: $1656/1671 = 0.45$ for DEW, $1657/1673 = 0.51$ for HEW, and $1649/1665 = 0.27$ for HYW. This represents the values of 37%, 42%, and 22% of water/collagen interactions, showing that for HYW the compactness of the collagen fiber bundles is higher than in DEW and HEW. We can translate this observation and state that the HYW group has a lower water content in the collagen triple helix than the DEW and HEW groups, and with the lower quantities in the DEW volunteers. Carbonyl stretching ratios in the H.P.P, H.P.P.4H₂O, and H.P.P.H₂O systems representing the calculated Amide I band found for young, elderly, and diabetic elderly women indicates the calculated relative Raman intensity ratios.

Table 2: Carbonyl stretching ratio in the HP.P, HPP.4H₂O, HP.P.H₂O system representing the calculated Amide I band found for young, elderly, and diabetic elderly women. (*) indicates the calculated relative Raman Intensity ratio.

Systems	Exp. Wn. And ratios	Calc. wn and ratios
HYW: HP.P	1649/1665 0.23/0.84 = 0.27	1619/1674 0.52; 0.57*
HEW: HPP.4 H ₂ O	1658/1673 0.30/0.59 = 0.51	1621/1680 1.69; 1.69*
DEW: HP.P.H ₂ O	1650/1671 0.29/0.65 = 0.45	1620/1709 0.97; 1.12* (water near carboxilate of HP)
DEW: HP.P.H ₂ O	1650/1671 0.29/0.65 = 0.45	1583/1711 1.21/...* (water near the -C=O group of P)

iv) Spectrum of the Differences

In our studies on the dermal water content among healthy elderly women, diabetics and healthy young women [11], the software that controls the confocal Raman spectrophotometer determines the water content taking into account the spectral region of the CH stretch bands, as well as a band in the spectral region above 3000 cm⁻¹. If another Raman spectrophotometer were used to conduct such studies, it would not be possible to use the software provided by Rivers Diagnostic. Between 3000 - 3750cm⁻¹, in both the Raman and the infrared spectra, the band representing the normal OH stretching mode is broad and intense. Within the profile of this band, the bands of combinations and overtones of chemical bonds and of the characteristic chemical groups are hidden, as well as the symmetrical and antisymmetric stretching bands of the primary amines. Since we wanted information about the dermal water content, we determined the average spectrum of each group and chose the spectral region mentioned above. We then recorded the Raman spectrum of pure water according to the following specifications: Milli-Q ultrapure water (Millipore Durect-Q3 water purification System) as a reference. Two drops of Milli-Q ultrapure water (0.07mL) were placed on a confocal Raman lens (with an area of 6cm²), corresponding to 12 microliters per cm². The measurements were performed in the spectral region classified as high-frequency (2500 - 4000cm⁻¹). The same parameters were used for the three groups of participants (healthy young, diabetic and non-diabetic elderly women).

Subsequently, the spectrum of the pure free water was subtracted from the Raman spectra of each set of samples. The process of subtraction was performed using the Omnic software from Spectra Thermo Fisher (US, USA) [22], which was also used to determine the second derivative spectra and the Fourier self-deconvolution spectra (FSD) that we employed to find out the hidden bands below the band profile in the 3150 - 3700cm⁻¹ region. Figure 4 illustrates the result of such procedure.

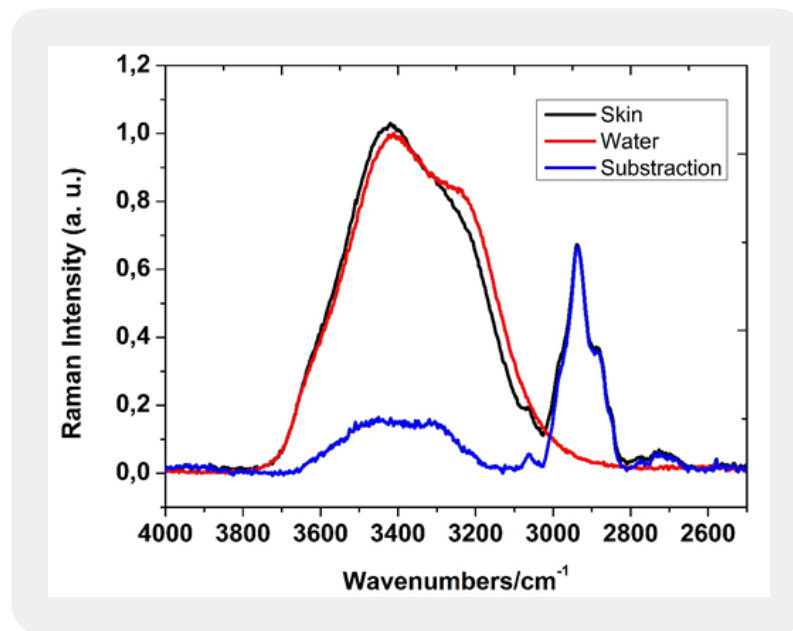


Figure 4: Mean Raman spectrum of the skin of elderly diabetic women (black), the average Raman spectrum of Milli-Q water (red), and the result of the difference between the two spectra (blue).

Figure 5 shows the band profile resulting from the subtraction of pure water from the second spectral derivative, as well as the band profile generated by the FSD.

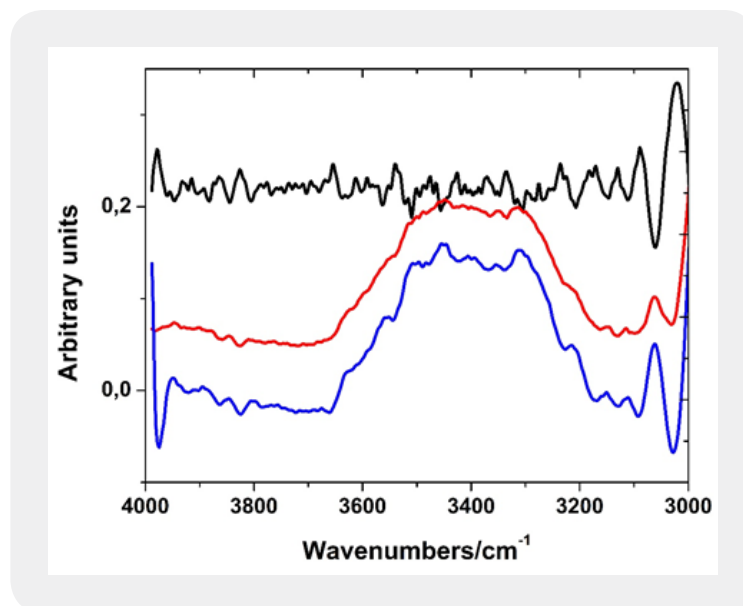


Figure 5: The black line represents the second derivative of the average Raman spectrum of the skin of elderly diabetic women (EDW). The red line is the actual Fourier self-deconvolution (FSD) and the blue line is the result of the subtraction between the mean spectrum of EDW and the water spectrum.

As results in Table 3 we present the vibrational assignment of the second derivative (or FSD bands) in the 3150-3700 cm⁻¹ region of the mean Raman spectra of elderly diabetic women.

Table 3: Second derivative bands (or FSD bands) in the in the 3150–3700 cm⁻¹ region of the mean Raman spectra of elderly diabetic women

Band position. cm ⁻¹	Assignment
3634	v(OH) attached water
3602	v(OH) attached water
3579	v(OH) attached water
3563	v(OH) attached water
3513	v(OH) attached water
3491	v _{as} (NH)(NH ₂)
3475	v _{as} (NH)(NH ₂)
3453	v(NH) secondary amide
3415	v(NH) histidine
3401	v _s (NH)(NH ₂)
3387	v _s (NH)(NH ₂)
3361	v _{as} (NH)(NH ₂)
3315	1653 + 1668 = 3321 ; v _a (NH)(NH ₂)
3287	v _s (NH)(NH ₂)
3251	v _s (NH)(NH ₂)
3211	1554 + 1653 = 3207
3148	v(NH) bonded secondary amide
v _s = 345.5 + 0.876(3491) = 3404 cm ⁻¹	observed at 3401 cm ⁻¹
v _s = 345.5 + 0.876(3475) = 3390 cm ⁻¹	observed at 3387 cm ⁻¹
v _s = 345.5 + 0.876(3361) = 3290 cm ⁻¹	observed at 3287 cm ⁻¹
v _s = 345.5 + 0.876(3315) = 3249 cm ⁻¹	observed at 3251 cm ⁻¹

Bellamy-Williams equation for primary amines. Ex. Subtraction spectra between EDW and water [23].

Figure 6 summarizes the results obtained using the procedure described above for the three groups of participants. Notice that the DEW value of 33.47% reflect the glucose action according his higher water solubility in the triple helix chanel.

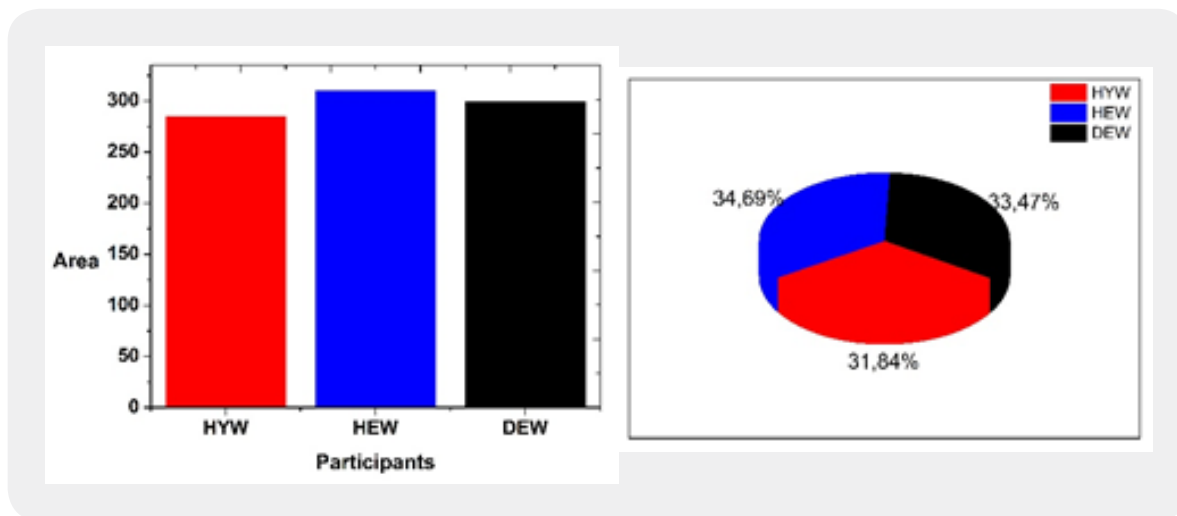


Figure 6: Left: Graphical representation of areas $[R_i \times \omega_n]$ determined for the Raman bands in the 3515–3700 cm^{-1} region for healthy young women (HYW), healthy elderly women (HEW), and diabetic elderly women (DEW). Right: Graphical representation of the area in percentage for HYW (31.84%), HEW (34.69%), and DEW (33.47%).

v. IR Measurements. Enhanced Infrared Absorbance Using a Cooper Sheet of $\pm 45 \mu m$.

As the increased factor of infrared absorption is several units of magnitude lower in comparison to the SERS effect, the Surface Enhanced Infrared Absorption Spectroscopy (SEIRA) effect has been less studied. The first work on the SEIRA effect is by A. Hartstein *et al* [24]. The paper by Osawa [25] provides an excellent review on the SEIRA effect and, in the summary, Osawa states that molecules which are absorbed on films of metal island particles exhibit infrared absorption between 10 - 1000 times greater than ordinary infrared records. In our case, we obtained an absorption increase of the order of 400%.

In order to characterize the copper sheet, we used a Scanning Electron Microscope (SEM) from Zeiss (EVO MA 10). The thickness of the copper sheet oscillated between 42.05 and 48.79 μm .

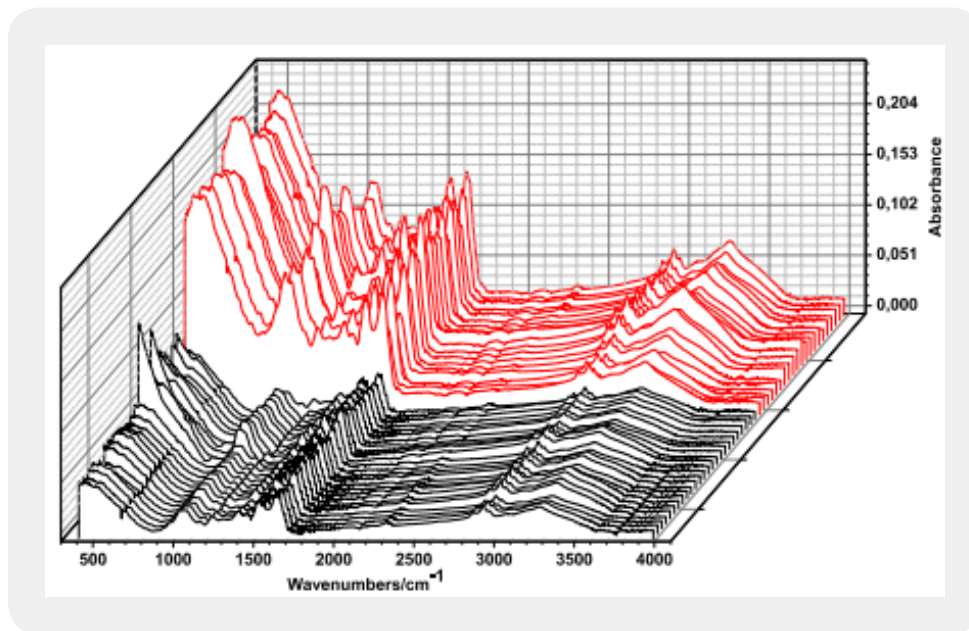


Figure 7: ATR spectra of the multi-sensitive bacteria of the genus *Klebsiella* measured on a glass slide (black) and on a copper sheet (in red) of $\pm 45\mu\text{m}$. Deposits of the lyophilized sample.

Figure 7 shows the increase in the absorbance of the infrared spectra (FT-IR), according to what was recorded for the bacteria samples on the $\pm 45\mu\text{m}$ copper plate (red) and on a glass plate used to collect the samples (black). Observing the absorbance scale we can appreciate an enhancement around 400 for the samples deposited on a thin copper sheet.

vi. Combined *in vivo* Confocal Raman Spectroscopy and DFT

In the paper “Combined *in vivo* confocal Raman spectroscopy and density functional theory to detect carboxymethyl(lysine) in the human stratum corneum” [6], in order to identify the presence of the glycation product carboxymethyl(lysine), we recorded the confocal Raman spectra of the stratum corneum from a set of volunteers. Next, we calculated the mean value of these spectra and their second derivative. The next step was to obtain the CML spectrum by means of theoretical calculations based on the Density Functional Theory (DFT), using the B3LYP functional with basis set 6-311G (d, p). After correcting the harmonic spectrum, it was compared with the second spectral derivative of the average spectrum of the stratum corneum. Spectral coincidences indicated the present CML bands. Figure 8 presents the coincident bands between the second derivative mean value spectrum of the skin stratum corneum of the EDW group of participants, together with the experimental confocal Raman spectrum of CLM.

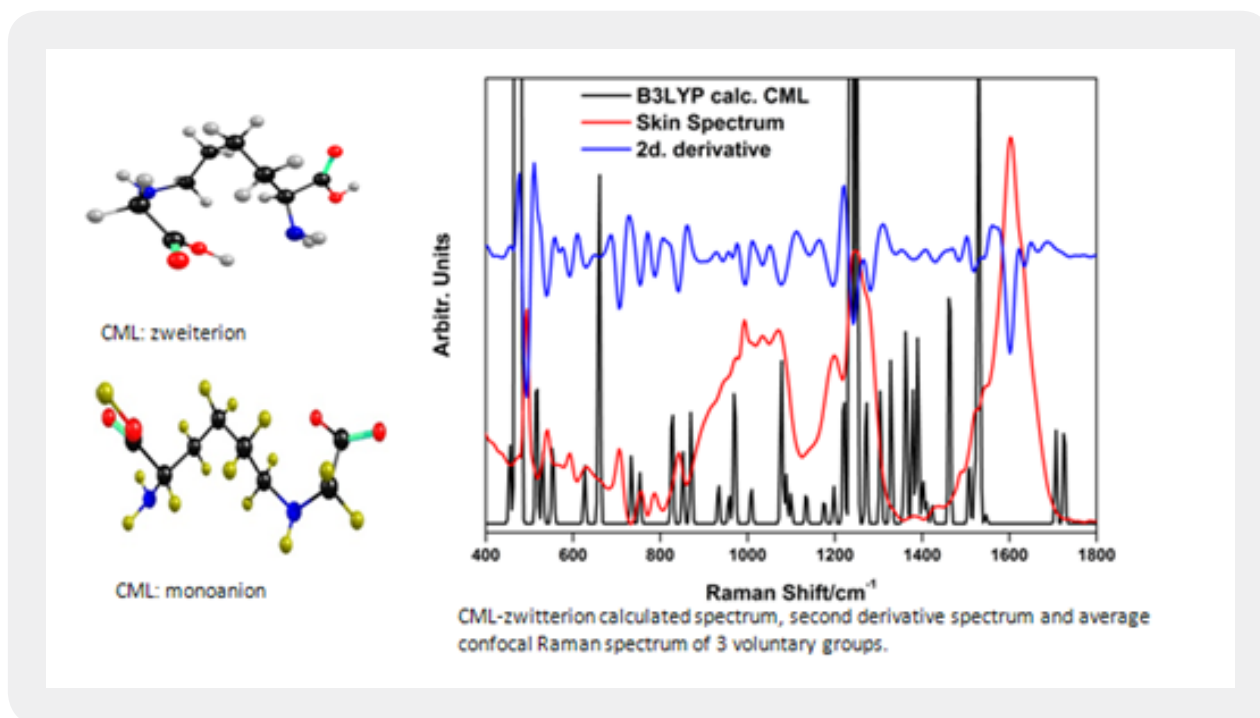


Figure 8: CML - zwitterion calculated spectra (Black), second derivative spectra and average confocal Raman spectra of the EDW voluntary group (blue and red, respectively)

Table 4 presents the 22 fundamental bands of carboxymethyllysine with their respective areas as present in the confocal Raman spectra of the three groups of voluntaries. The band areas were obtained by the deconvolution band procedure.

Table 4: Areas of the 22 bands of carboxymethyllysine present in confocal Raman spectra of three groups of participants.

Wavenumber [cm ⁻¹]	Young women (Band area) [I _R x cm ⁻¹]	Elderly Women (band area) [I _R x cm ⁻¹]	Diabetic Elderly women (band area) [I _R x cm ⁻¹]
1466		0.81	0.60
1449	0.35	0.17	0.18
1440	0.73	0.77	1.05
1341	13.15	13.57	14.07
1321	2.82	3.800	2.82
1304	7.65	5.91	6.94
1295	1.21	1.32	1.21
1282	1.77	2.48	2.24

1249	3.00	2.31	2.34
1208	0.66	1.33	0.82
1157	0.88	0.92	0.90
1085	0.97	0.88	0.78
1062	0.65	0.64	0.55
971	0.13	0.12	0.04
959	0.10	0.13	0.11
865	0.54	0.52	0.55
854	0.44	0.46	0.42
757	0.31	0.33	0.23
728	0.51	0.39	0.44
669	0.30	3.18	0.14
622	0.44	0.39	0.44
609		7.09	0.10
Sum and %	36.61 (30%)	47.51 (39%)	36.96 (31%)
Average value	1.66	2.16	1.68
Standard deviation	3.06	3.17	3.15
Standard error	0.65	0.67	0.67

VII) Study of Lympho Nodes Using Statistical Procedures, Spectral Subtraction and Self Enhanced Raman Spectra (SERS)

Among the lymphoid organs, there are the lymph nodes, which are considered as lymph filters because they are rich in lymphocytes and other defense cells. Among the factors that contribute to their impairment, we note the invasion of its structure by neoplastic cells. Cytology is the gold-standard diagnostic test, and FNA is the most used technique to obtain the material to be analyzed. However, some studies question its use, due to the loss of cellular architecture. Confocal Raman spectroscopy, through its ability to utilize biochemical differences in tissues and cells, has been increasingly prominent in this type of diagnosis. The study aimed to identify the main biochemical characteristics in normal and compromised lymph nodes and cervical lesion using confocal Raman spectroscopy. We analyzed 12 normal and altered lymph node samples from patients with medical indications for a lymphadenectomy by spectroscopy, followed by statistical analysis of the main components (PCA) and linear discriminant analysis (LDA). After the analysis, it was observed that this technique was able to discriminate the tissues with values of specificity, sensitivity and accuracy of up to 83%. Therefore, confocal Raman spectroscopy has been shown to be an important tool in the characterization of lymph nodes, and in the future it may help in the diagnosis of lymph node lesions.

In the statistical analysis, we first used the OriginPro 8 software [26] to obtain the mean and standard deviation spectra for all samples in the region between 900 and 1800 cm⁻¹. Next, we used the Minitab® software [27] to classify the spectra according to the Principal Component Analysis (PCA), a statistical

method that separates the original variables of a group according to their similarities from the analysis of the scatterplot associated to the loading plot, and according to supervised methods such as Linear Discriminant Analysis (LDA). In addition, we determined the sensitivity, specificity, and accuracy values of the test by means of a contingency matrix based on the values found by the PCA analysis associated with the histopathological results.

From the loading plot, we obtained the main peaks and attributions that were identified for the normal and compromised lymph node groups. Comparative spectra are shown in Figure 9, and Table 5 presents the band assignment for the two kinds of tissues.

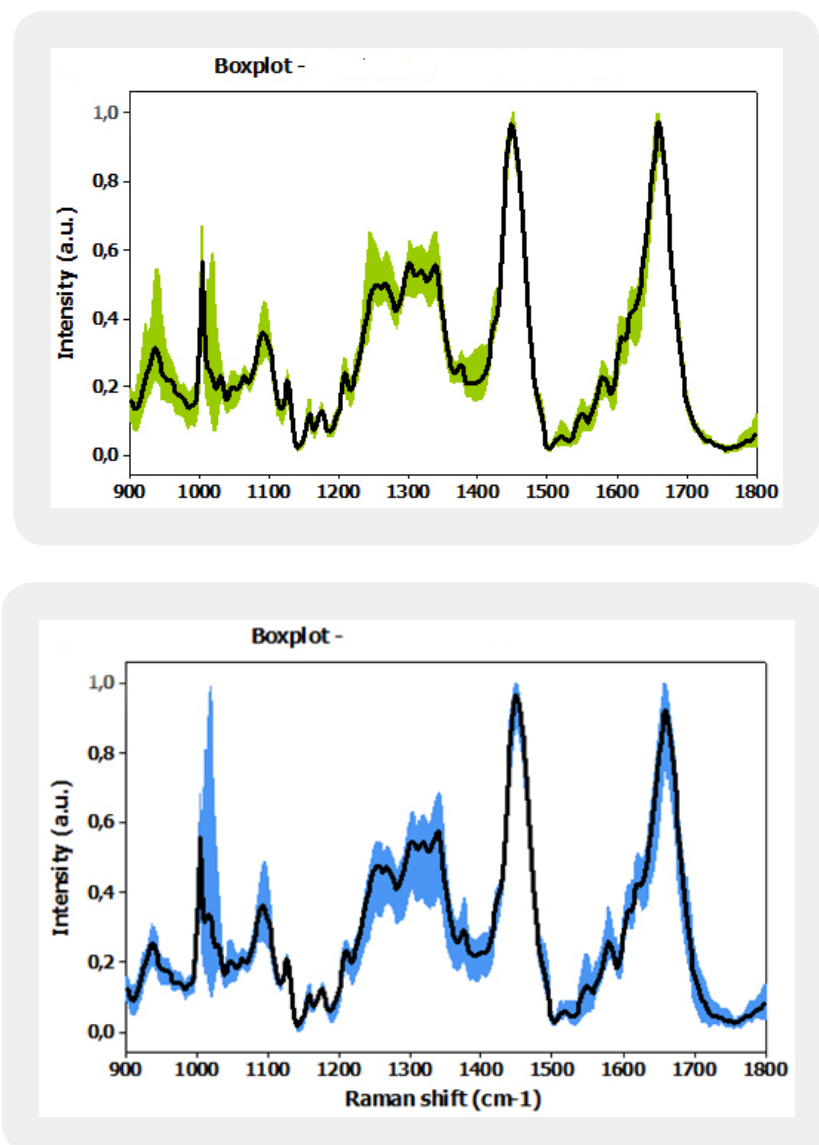


Figure 9: Average spectrum with standard deviation for the analyzed groups. Down: Normal lymph node group. Up: Involved lymph node group

Table 5: Main peaks and attributions identified for normal and compromised lymph node groups from the loading plot. Values in cm^{-1} .

Normal Lymph nodes	Abnormal tissue	Assignment
	970	proteins and nucleic acids
928		v(C-C), stretching - probably in proline and valine amino acids (protein band)
1032		CH ₂ CH ₃ collagen and phospholipid twisting modes, C-C stretching, collagen phenylalanine
1104		phenylalanine
1150		glycogen
	1168	lipids
1184		phosphate vibrations
	1224	proteins, including type I collagen, and amide III
1210		C-C6H ₅ stretching mode in tyrosine and phenylalanine
	1256	DNA / RNA, amide III
1302		collagen, phospholipids, lipids, amide III
1330		typical phospholipids, DNA region, collagen, nucleic acids and phosphates
	1362	tryptophan, guanine
1498		C=C stretching in a benzene ring
	1521	carotenoids (absent in normal tissues)
	1556	tryptophan, amide II, tyrosine
1630		Amide I
	1662	Lipids and Nucleic Acids v: stretching vibrations. Wavelength with a confidence interval of $\pm 2\text{ cm}^{-1}$.

Movasaghi, Z.; Rehman, S.; Rehman, I.U. Infrared Raman Spectroscopy of Biological Tissues, Applied Spectroscopy Reviews, 42:5, 493-541, 2007 [28].

At the EMBRAER Congress realized in Campos de Jordão (SP), Brazil (2018), we presented a work on normal and abnormal tissues of lymph nodes, focusing our attention in the SERS effect [3].

First, we took the Raman spectrum by depositing the sample on a glass slide. Then, on another slide, we deposited a thin layer of chitosan and recorded its spectrum in order to subtract it later. We placed silver nanoparticles on the top of chitosan [29]. Next, we placed the compromised tissue sample and record the SERS spectra. The obtained spectra are shown in Figure 10. Despite indicating the spectral differences

between tissues, we concluded that confocal Raman spectra treated by statistical procedures do not provide the broad and impressive information provided by SERS.

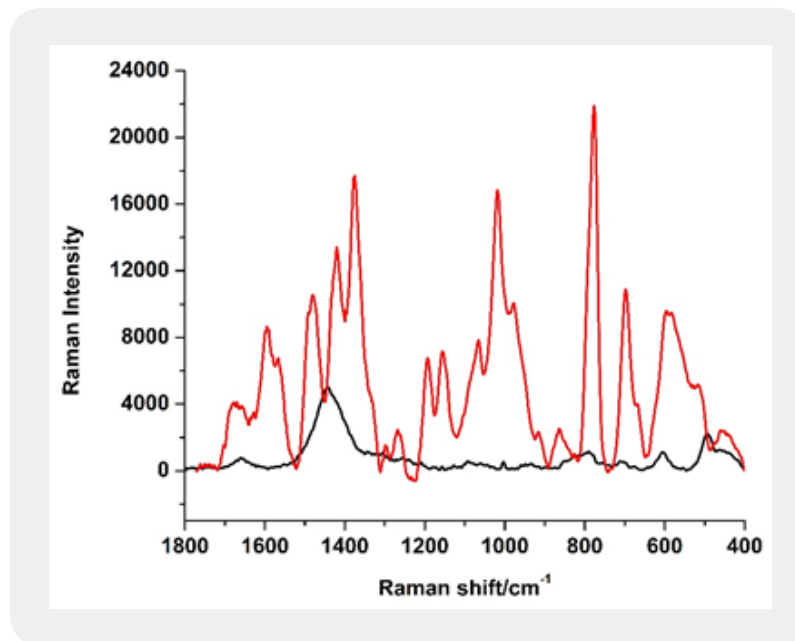


Figure 10: Raman spectrum of compromised lymph node (black). In red, the SERS effect for the same sample.

In Table 6 we present the observed SERS bands of the abnormal lymph node.

Table 6: SERS spectrum of abnormal lymph node.

Wavenumber/cm ⁻¹	Approximate assignment	Wavenumber/cm ⁻¹	Approximate assignment
1758	One of absorption positions for the C=O stretching vibrations of cortisone	1330	Typical phospholipids, Region associated with DNA & phospholipids, Collagen, Nucleic acids and phosphates
1695	Amide I (turns and bands)	1289	Phosphodiester groups in nucleic acids
1688	Amide I (disordered structure; non hydrogen Bonded)	1244	Amide III
1684	Amide I (disordered structure; non hydrogen Bonded)	1213	C-C6H5 stretching mode in tyrosine and Phenylalanine

1678	Bound & free NADH	1135	
1673	Amide I	1096	Phosphodioxy (PO ₂ ²⁻) groups
1666	Collagen	1087	
1662	Nucleic acid modes (1) Nucleic acid modes indicating the nucleic acid content in tissues	1043	Carbohydrates peak for solutions and solids (3) Proline (collagen assignment)
1657	Fatty acids (2, 3) Amide I (collagen assignment) (74) Triglycerides (fatty acids)	1020	Glycogen
1652	Lipid (C55C stretch)	1006	Carotenoids (absent in normal tissues), Phenylalanine, d(ring)
1641	Amide I band (protein band)	958	
1631	Amide I	930	Carbohydrates peak for solutions and solids
1621	(C=C), porphyrin	918	Proline, hydroxyproline, Glycogen and lactic acid
1602	Phenylalanine	898	Monosaccharides (β-glucose), (C-O-C) skeletal Mode
1586	Phenylalanine, hydroxyproline	859	C ₃ endo/anti (A-form helix) conformation
1581	(C=C), phenylalanine, Phenylalanine	808	Phosphodiester (Z-marker)
1576	Nucleic acid mode (1) Nucleic acid modes indicating the nucleic acid content in tissues	728	C-C stretching, proline (collagen assignment)
1565	Ring base	657	
1547	Tryptophan	631	C-S gauche (amino acid methionine)
1459	Deoxyribose, bending (CH ₂)	590	Symmetric stretching vibration of n ₄ PO ₄ ³⁻ (phosphate of HA)

1447	CH ₂ bending mode of proteins & lipids (66) CH ₂ deformation (protein vibration)-A marker for protein concentration	567	
1426	Deoxyribose, (B,Z -marker)	555	
1393	CH rocking	509	S-S disulfide stretching band of collagen (31) n(S-S) gauche-gauche-gauche (aminoacid cysteine)
1386	CH ₃ bending	498	
1378	CH ₃ bending	464	
1360	Tryptophan	449	Ring torsion of phenyl
1354	Guanine (N7, B, Z-marker)	434	
1348	Bending HCH		

Conclusion

Comparatively, the statistical treatment provides only eight bands that differ from the spectrum of healthy lymph nodes, however, by the SERS effect, according to the measurement techniques that we have indicated, we obtained 55 bands, of which only three of them were coincident with the spectrum generated by the statistical procedure. Statistical procedures are excellent to deal with the goodness of the data and to point out differences between different sets of measurements, however, they are unsatisfactory to predict the numerical magnitude of a vibrational spectrum, even more if in this measurement techniques that lead to an increase in the intensity of the bands are used, such as like the SERS (Raman) and SEIRA (infrared) effects, or another equivalent like the one we present in this review.

Disclosures of Interests

The authors have no financial interests in this article and declare no conflict of interest.

Acknowledgments

C. A. Téllez, thanks to FAPESP (process number 2019-00558- 8).

Bibliography

1. Téllez Soto, C. A., Medeiros-Neto, L. P., dos Santos, L., Santos, A. B.O., Ferreira, I., *et al.* (2018). Infrared and confocal Raman spectroscopy to differentiate changes in the protein secondary structure in normal and abnormal thyroid tissues. *J Raman Spectrosc.*, 49(7), 1165-1173.

Claudio Téllez Soto, A., *et al.* (2022). Vibrational Spectroscopy Techniques Used in the Analysis of Glycation Products, Water Content in the Dermis of Diabetic Elderly, Healthy Young, Healthy Elderly Women, and in the Interpretation of Goiter, Follicular and Papillary Thyroid Cancer. *CPQ Medicine*, 13(1), 01-22.

2. dos, J. S. Corrêa, L. P. M. Neto, M. J. Chagas, A. P. C. Ferreira, *et al.* (2017). Lymph node study by confocal Raman spectroscopy. *O Mundo da Saúde*. 41(1), 30-39.
3. Téllez-Soto, C. A., Neto, L. P. M., dos, J. S., Corrêa, A. & Martin, A. (2017). Espectro Raman Aumentado por Superfície (SERS) de Linfonodos. V Encontro Brasileiro de Espectroscopia Raman V EnBraER 03 a 06/12/17. Campos do Jordão - SP.
4. Corrêa, dos, J. S., Neto, L. P. M., Santos, L. dos, de Carvalho, L. F., *et al.* (2016). Caracterização bioquímica de linfonodos normais, comprometidos e lesões cervicais por Espectroscopia. *Revista Univap*, 22(40), 141.
5. Medeiros Neto, L. P., das Chagas e Silva de Carvalho, L. F., dos Santos, L., Tellez Soto, C. A., *et al.* (2017). Raman spectroscopic analysis of oral cells in the high wavenumber region. *Photodiagnosis Photodyn. Ther.*, 103(3), 255-262.
6. Téllez-Soto, C. A., Mendes, T. O., dos Santos, L., Silva, M. G. P., Pinto, L. P., *et al.* (2019). Combined *in vivo* confocal Raman spectroscopy and density functional theory to detect carboxymethyl(lysine) in the human stratum corneum. *Vibrational Spectroscopy*, 100, 40-47.
7. Pereira, L., Téllez-Soto, C. A., Santos, L., Ali, S. M., Fávero, P. P. & Martin, A. A. (2015). Confocal Raman study of aging process in diabetes mellitus human voluntaries SPIE. (Pp.1-9).
8. Téllez-Soto, C. A., Pereira Pinto, L., Santos, L., Fávero, P. & Martin, A. A. (2015). RM1 semi empirical and DFT: B3LYP/3-21G theoretical insights on the confocal Raman experimental observations in qualitative water content of the skin dermis of healthy young, healthy elderly and diabetic elderly women's. *Spectrochim Acta A. Mol Biomol Spectrosc.* (149), 1009-1019.
9. Liliane Pereira, Claudio Téllez, A. S., Priscila Fávero & Airton Martin, A. (2017). Confocal Raman Spectroscopic Analysis of the Changes in Type I Collagen Resulting from Amide I Glycation. *BJSTR.*, 1(3), 1-7.
10. Téllez-Soto, C. A., Pereira Silva, M. G., dos Santos, L., de O. Mendes, T., Singh, P., *et al.* (2020). *In vivo* determination of dermal water content in chronological skin aging by confocal Raman spectroscopy, *Vibrational Spectroscopy*, 112(103196).
11. Isamara Tanaka, Claudio Téllez-Zepeda, A., Rogerio Philippov, Priscila Fávero, Airton Martin, A. & Claudio Téllez-Soto, A. (2018). Enhanced Infrared Absorption in a Comparative Study between Multi-Sensitive and Multiresistant Bacteria of the Genus *Klebsiella* sp. *Vibrational Spectroscopy*, 96, 83-92.
12. Fukunaga, K. (1990). Introduction to Statistical Pattern Recognition. Academic Press, San Diego, California.
13. Hyperchem (TM) Professional 7.51, Hypercube, Inc., 1115 NW 4th Street, Gainesville, Florida 32601, USA.

14. Gaussian 03, Revision C.02. M.J. Frisch, G.W. Trucks, H.B. Schlegel, G.E. Scuseria, M.A. Robb, J.R. Cheeseman, *et al.* (2004). Gaussian, Inc., Wallingford, CT.
15. Chemcraft: Graphical program for working with quantum chemistry computations. 2016. v.1.8.
16. Gallagher, W. (1997). FTIR Analysis of Protein Structure. *Biochemistry*, 392, 662-666.
17. Dong, A., Huang, P. & Caughey, W. S. (1990). Protein Secondary Structures in Water from Second-Derivative Amide I Infrared Spectra. *Biochemistry*, 29(13), 3303-3308.
18. Barth, A. & Barth, A. (2007). Infrared spectroscopy of proteins. *Biochim Biophys Acta Bioenerg.*, 1767(9), 1073-1101.
19. Kong, J. & Yu, S. (2007). Fourier transform infrared spectroscopic analysis of protein secondary structures. *Acta Biochim. Biophys. Sin. (Shanghai)*, 39(8), 549-559.
20. Chirgadze, Y. N. & Nevskaya, N. A. (1976). Infrared spectra and resonance interaction of amide-I vibration of the antiparallel-chain pleated sheet. *Biopolymers*, 15(4), 607-625.
21. Nguyen, T. T., Hapillon, T., Feru, J., Brassart-Passco, S., Angiboust, J. F., *et al.* (2013). Raman comparison of skin dermis of different ages: focus on spectral markers of collagen hydration. *Journal of Raman Spectroscopy*, 44, 1230-1237.
22. Nicolet iS-10 FT-IR Spectrometer with Continuum Infrared Microscope. In: Arcade, software OMNIC from Thermo-Nicolet, NY, USA.
23. Bellamy, L. J. & Williams, R. L. (1957). The NH stretching frequencies of primary amines. *Spectrochim Acta*, 9(4), 341-345.
24. Hartstein, A., Kirtley, J. R. & Tsang, J. C. (1980). Enhancement of the Infrared Absorption from Molecular Monolayers with Thin Metal Overlayers. *Phys. Rev. Lett.*, 45(3) 201-204.
25. Osawa, M. (1997). Dynamic processes in electrochemical reactions studied by Surface-Enhanced-Infrared Absorption Spectroscopy (SEIRAS). *Bull. Chem. Soc. Jpn.*, 70(12), 2861-2880.
26. Origin Pro 8.0: Software. Origin Lab. Corporation, Northampton, MA. USA.
27. Minitab 17 Statistical Software (2010) [Computer software]. State College, PA: Minitab.
28. Movasaghi, Z., Rehman, S. & Rehman, I. U. (2007). Raman Spectroscopy of Biological Tissues. *Applied Spectroscopy Reviews*, 42(5), 493-541.
29. Xi-Feng Zhang, Zhi-Guo Liu, Wei Shen & Sangiliyandi Gurunathan (2016). Silver Nanoparticles: Synthesis, Characterization, Properties, Applications, and Therapeutic Approaches. *Int J Mol Sci.*, 17(9), 1534.

Claudio Téllez Soto, A., *et al.* (2022). Vibrational Spectroscopy Techniques Used in the Analysis of Glycation Products, Water Content in the Dermis of Diabetic Elderly, Healthy Young, Healthy Elderly Women, and in the Interpretation of Goiter, Follicular and Papillary Thyroid Cancer. *CPQ Medicine*, 13(1), 01-22.